International Journal of Automation and Control

ISSN online: 1740-7524 - ISSN print: 1740-7516
https://www.inderscience.com/ijaac

Contamination detection in the cultivation of leukocyte based on image sparsity evaluation

Lianghong Wu, Zhiyang Li, Liang Chen, Cili Zuo, Hongqiang Zhang

DOI: 10.1504/IJAAC.2025.10062262

Article History:

Received:	15 September 2023
Last revised:	04 December 2023
Accepted:	01 January 2024
Published online:	02 December 2024

Contamination detection in the cultivation of leukocyte based on image sparsity evaluation

Lianghong Wu*, Zhiyang Li, Liang Chen, Cili Zuo and Hongqiang Zhang

School of Information and Electrical Engineering,
Hunan University of Science and Technology,
Xiangtan, 411201, China
Email: lhwu@hnust.edu.cn
Email: 398745765@qq.com
Email: kentchen@163.com
Email: cilizuo@163.com
Email: hongqiangzhang@hnust.edu.cn
*Corresponding author

Abstract: The contamination in the cultivation of cells seriously affects the reliability and reproducibility of experimental results. Currently, the detection of contamination in cells relies heavily on manual observation, which is labour-intensive and time-consuming. In this paper, it proposes a sparse matrix clustering (SMC) method based on the principle of matrix sparsity to automatically detect the contamination in leukocytes. Firstly, the image segmentation and local adaptive binarisation techniques are used to eliminate the noise points and shadows. Then, a scoring map of image sparsity based on the pixel distribution of segmented images is proposed to index the pollution degree of the leukocyte. By dynamically determining the threshold for evaluating image sparsity based on the maximum distributed pixels on the scoring map, the image sparsity is used as a feature for contamination classification. Experimental results show that this method achieves an accuracy of 98.8% for detecting contamination in leukocyte culture images with fast detection speed, which can be used as an efficient cell contamination detection approach in the biomedical field.

Keywords: image sparsity evaluation; image segmentation; local adaptive binarisation; leukocyte contamination; sparse matrix clustering; contamination detection; image feature extraction; image classification.

Reference to this paper should be made as follows: Wu, L., Li, Z., Chen, L., Zuo, C. and Zhang, H. (2025) 'Contamination detection in the cultivation of leukocyte based on image sparsity evaluation', *Int. J. Automation and Control*, Vol. 19, No. 1, pp.18–36.

Biographical notes: Lianghong Wu received his BSc in 2001 from Hunan University of Science and Technology (former Xiangtan Institute of Technology), received his MSc in 2007 from Hunan University, received his PhD in 2011 from Hunan University, now he is a Professor in Hunan University of Science and Technology. His main research interests include intelligent optimisation algorithms and applications, multi-objective optimisation, intelligent control theory and swarm robot systems and control.

Zhiyang Li received his BSc in 2020 from Hunan University of Science and Technology. He is currently a Master student at Hunan University of Science and Technology. His main research interests include medical image processing, image deep learning and machine vision.

Liang Chen, PhD, graduated from Harbin Engineering University in 2012 majoring in navigation, guidance and control. He is currently a Lecturer in the Department of Automation, School of Information and Electrical Engineering, Hunan University of Science and Technology. He is mainly engaged in machine vision, underwater robot detection and so on.

Cili Zuo received his PhD in Control Science and Engineering from the East China University of Science and Technology, Shanghai, China, in 2021. He is currently a Lecturer with the College of Information and Electrical Engineering, Hunan University of Science and Technology. His research interests include signal processing, pattern recognition, machine learning, computational intelligence, and brain-computer interface.

Hongqiang Zhang received his BS, MS and PhD in Control Science from Hunan University of Science and Technology in 2001, Hunan University (HNU) in 2004 and HNU in 2016, respectively. He is currently a Lecturer with the School of Information and Electrical Engineering, Hunan University of Science and Technology, Xiangtan, China. His research interests are swarm robotics system, swarm intelligence, optimisation, and intelligent control.

1 Introduction

Cell proliferation techniques in vitro, also known as cell culture, are widely used in scientific research, teaching, clinical trials, preparation of biological products, and other fields. However, contamination can occur during cell cultivation due to improper sampling, careless operation, or inadequate sterilisation. Cell contamination leads to severe consequences, including waste of time and research funds, erroneous experimental data, and irreproducible experiments. Bacterial and fungal contaminations often occur after open operations such as passage, medium change, and medium addition. Moreover, due to their rapid growth, most contaminations become apparent within 48 h after occurrence. Therefore, closely observing experimental samples within the first 48 h of the experiment to take remedial measures or eliminate contaminations is critical (Mani et al., 2023; Mahmood and Ali, 2017). Thus, the key to ensuring the purity of cultured cells is to promptly and accurately determine whether the cultured cells are contaminated. The primary method to judge cell culture contamination is manual observation under a microscope (Ray et al., 2021). Although this method can provide a high accuracy, its high labour cost and inability to ensure timely contamination detection are concerning. Therefore, rapid and accurate screening of contaminated cell cultures is essential for the biomedical industry.

There are various types of cell contamination, such as bacterial, fungal, mycoplasma, viral, insect, parasite, chemical, and cell cross-contamination. Different contamination sources lead to different characteristics in the culture medium. For example, bacterial contamination makes the medium turbid with colour change and rapid pH shift. Contaminated adherent cells will gradually detach from the wall and die within days.

Fungal contamination causes a slower cell growth and the formation of white, light yellow, or black spots in the medium. Therefore, a preliminary determination of whether the cell is contaminated with bacteria or fungi can be made by observing the medium's colour, floaters, and pH or by observing the cells and their growth state under the microscope (Brînzeu et al., 2008). Thus, the key to achieving image-based cell contamination detection is to extract the above visual features.

The cell image datasets in experiments suffer from problems of few samples, uneven illumination, blurring, and different cell manifestations across stages. The problems caused by insufficient samples have attracted researchers' attentions in recent years. Few-shot learning provides an effective solution to this problem, Liu et al. (2022) categorise few-shot learning image classification algorithms into four distinct groups based on variations in deep learning mechanisms. Through a comparative analysis of experimental results from representative algorithms, the performance, advantages, and disadvantages of each approach are examined. It demonstrates that existing few-shot learning algorithms yield promising outcomes in various application scenarios involving image classification tasks. Detection using deep learning is time-consuming, and the accuracy fluctuates. Traditional computer vision methods can avoid the problem of insufficient samples. Chen et al. (2022) used Information Entropy as a separation parameter combined with brightness histograms to determine segmentation thresholds for automatic separation. They achieved the final separation and extraction of target regions based on segmentation thresholds and entropy values. This method improved the efficiency and accuracy of image processing of paleontological dinosaur egg fossil CT images. However, it is difficult to find suitable segmentation thresholds for cell culture samples with uneven illumination and impure backgrounds. Bhowmik et al. (2018) presents a novel game theory inspired binarisation technique, and handled the problems of uneven illumination and complex shadows in experimental images. However, it is limited to image classification problems with explicit detection targets. In addition, Li et al. (2019) proposed spatial sparse coding and multiple instance learning (SSC-MIL) algorithm to solve the problem of criminal investigation image classification without clear detection targets; Celik (2009) used principal component analysis (PCA) to extract distinguishing and robust scale-invariant feature transform (SIFT) feature vectors from difference images for unsupervised classification; Sarowar et al. (2019) introduced an object recognition method based on histogram of oriented gradient (HOG) feature descriptor combined with PCA and support vector machine (SVM). Improve the efficiency and accuracy of object classification, and reduced the burden of calculation and cost. Gan et al. (2021) provides a detailed survey on existing Non-negative matrix factorisation (NMF) methods, including a comprehensive analysis of their design principles, characteristics and drawbacks. It also discusses various variants of NMF methods and analyses properties and applications of these variants. Lu and Li (2022) proposed a clustering framework based on deep autoencoders, using multilayer perceptrons as encoders and decoders of the autoencoders, and *K*-means algorithm to cluster the feature vectors of the autoencoders, achieving unsupervised image classification.

Although the above methods perform well in various scenarios, they still have limitations. It cannot be processed in the face of complex cell images such as bacteria which are too small to constitute the detection target as the source of contamination and low noise contrast. In order to solve the above problems, this paper proposes a method of sparse matrix clustering (SMC) based on matrix sparsity to detect leukocyte cell

contamination. The underlying idea is to treat blank backgrounds in images as sparse matrix elements by combining image position encoding. The sparseness features of image blocks and reconstructed images are extracted to reduce the statistical correlation between transformed images and shallow features, minimise redundant information among feature vectors, and improve classification accuracy. Experiments on datasets obtained from the laboratory verified the method through *K*-means clustering. The results show that the proposed image sparsity evaluation method is far superior to other image processing algorithms like PCA and its variants regarding accuracy, clustering effects, and efficiency.

The rest of this paper is organised as follows. Section 2 then describes the proposed SMC method, including the theories and implementation procedures of image segmentation, scoring map calculation, and classification. Section 3 presents the experimental setup, results, and analysis of leukocyte cell images, comparing the performance of SMC with several representative methods. Section 4 summarises the conclusions and significance of this study and points out future directions for improving cell contamination detection performance.

2 Sparse matrix clustering

This paper proposes a cell contamination detection method based on block image sparsity evaluation. This method divides the image into sub-images with suitable proportions. Local adaptive binarisation of the sub-images is used to eliminate large noise blocks and shadows. Subsequently, the matrix sparsity is utilised to compute the background information of the sub-image, which is then reconstructed into a sparse scoring matrix (graph). The weighted average of the x most prominent maxima on the scoring matrix is taken as the binarisation threshold of the scoring matrix. The binarised scoring matrix result represents the image sparsity. As cell contamination levels exhibit unsupervised properties, we employ the *K*-means clustering algorithm as our classifier. Cell image sparsity and auxiliary features are normalised and input to the classifier to obtain the final classification results. The overall framework of the proposed contamination detection method is shown in Figure 1.

Figure 1 Framework of the proposed method (see online version for colours)

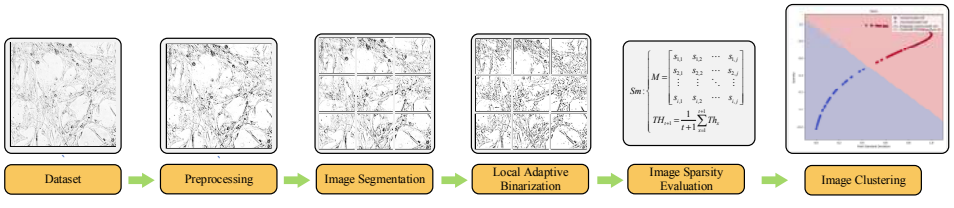

2.1 Preprocessing

Firstly, the greyscale processing is performed on the image. Leukocyte cell culture images lack usable colour information. The greyscale method can convert the image into a single-channel image, thus reducing computational complexity and increasing operation

speed. This paper adopts the classic optical formula for simple greyscale conversion, as shown in equation (1):

$$Y = 0.299 \times R + 0.587 \times G + 0.144 \times B \tag{1}$$

where Y is the final brightness value of the greyscale image point, R, G, and B are the values of the red, green, and blue channels of the colour image, respectively, and Y, R, G, B is in the range [0,255].

In the subsequent binarisation process of leukocyte cell culture images, the contaminated cell foreground contains fine suspended particles, which may be incorrectly identified as noise points and ignored. This problem can be solved by sharpening the image to enhance the edges and grey level transitions to improve the clarity of image contours (Shereena and Raju, 2022). By comparing the sharpening effects of 5 standard sharpening methods – Sharpening Filter, High-boost Filtering, Mean-Difference Filtering, and Unsharp Masking, Unsharp Masking retains many details without introducing too much noise, and the image clarity is higher without blurring. Therefore, Unsharp Masking was finally selected to sharpen the image. The principle of Unsharp Masking is to take the difference between the original image and its blurred version as sharpening details, amplify them, and add them back to the original image, as shown in equation (2):

$$U = G + a \times (G - B) \tag{2}$$

where U is the sharpened image, G is the greyscale image of the original image, a is a scalar parameter that controls the intensity of sharpening. The larger a is, the more prominent the sharpening details and the more precise the image. However, excessive a may lead to noise or over-sharpening. Therefore, a value should be determined according to image content and quality. Through comparative experiments of grid search with a step size of 0.5 within a reasonable range of parameters, it is determined that $a = 1.5$ works best in this paper. B is the blurred image obtained by Gaussian filtering of the original image.

2.2 Image segmentation

Although once contaminated by bacteria during leukocyte cell culture, a large amount of acidic substances will be produced in the medium, causing colour changes and significant turbidity in a short time (Mani et al., 2023), which is characterised by the reduction or disappearance of blank background. However, even without bacterial contamination, the viability of cultured cells will decline, undergo apoptosis or necrosis, and even detach and decompose over extended culture time, making it challenging to accurately capture the characteristics of an unpolluted blank background and increasing the likelihood of misjudgement. These blank backgrounds constitute a small proportion of the image and are sparsely distributed, making direct extraction difficult. Therefore, subtle differences in the overall blank background information of the image by capturing it are crucial to distinguishing the contamination status. To effectively obtain differences between local background information from polluted and unpolluted images, we employ block-based image processing techniques that enable accurate processing of detailed features while eliminating redundant interference information. The specific implementation process is as follows:

The preprocessed image, denoted as $X \in R^{a\times b}$, is subjected to grid segmentation with a block size of $n\times n$ and a stride of s. Consequently, $\frac{(a-n)(b-n)}{s^2}$ sub-image *Block* $B_i \in R^{n\times n}$ can be obtained, where a, b represent the pixel sizes of the image and $i \in \left\{1,2,\ldots,\frac{(a-n)(b-n)}{s^2}\right\}$. We set the stride $s=n$ to enhance computational efficiency by avoiding redundant calculations on blank backgrounds. The position encoding information of each image *Block*, including its row number r and column number c in the original image, is encoded by list $P=[(c_x,r_y)_1,(c_x,r_y)_2,\ldots,(c_x,r_y)_m]$ according to equation (3).

$$r_y=\left\lfloor\frac{pixel_y}{block_{height}}\right\rfloor, c_x=\left\lfloor\frac{pixel_x}{block_{width}}\right\rfloor \tag{3}$$

where $pixel_x, pixel_y$ are the coordinates of the top right pixel in the image block, $block_{width}=block_{height}=n$.

2.3 Local adaptive binarisation

Discrepancies in experiment duration and image-capturing angles during leukocyte cell culture experiments and image acquisition result in uneven illumination and shadow coverage, which can interfere with blank background information. Therefore, it is crucial to eliminate shadows and equalise brightness in images. Local adaptive threshold binarisation effectively addresses the issue of local brightness and shadow variations, providing density information of the foreground in sub-image *Block* and foreground shape details. The process of local adaptive binarisation is shown in Figure 2.

Figure 2 Image segmentation and local adaptive binarisation: (a) determine the binarisation path for the segmented binary images; (b) calculate the binarisation value using Gaussian distance weights; (c) generate the binarised image blocks sequentially along the path and (d) binaries the images (see online version for colours)

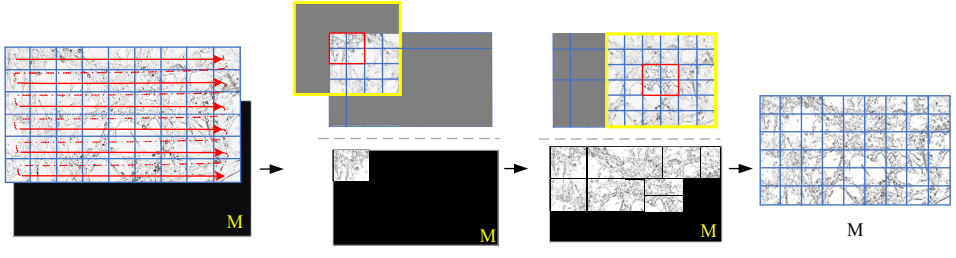

Based on the position encoding $P(i)$, determine the binarisation path $L(c_x,r_y)$. Let the greyscale value of the image at pixel (x,y) be $src(x,y)$, starting from the upper left corner $(0,0)$, scan each coordinate (x,y) in the order from left to right and top to bottom, and initialise the binarisation result image $M(x,y)$ as an all-zero matrix with the same size as the original image.

Calculate the Gaussian distance and threshold of $src(x,y)$ in the local window B. The size of the local window B is a crucial parameter of the local adaptive binarisation algorithm. Experiments show that when the neighbourhood range is four times the detection target, the retained local features and noise best affect image classification. Hence, the neighbourhood block size is taken as $B \approx 4 \times Block$ in this paper's algorithm. The standard deviation σ of the Gaussian window can then be calculated as equation (4) shows,

$$\sigma = 0.3 \times \left((B-1) \times 0.5 - 1 \right) + 0.8 \tag{4}$$

Taking $\mu_x = x, \mu_y = y$, the Gaussian weight w can be calculated by equation (5).

$$w(i,j) = \exp\left(-\frac{(i-x)^2 + (j-y)^2}{2\sigma^2} \right) \tag{5}$$

Then, according to the Gaussian weight, the local adaptive binarisation threshold can be calculated as equation (6),

$$T(x,y) = \frac{1}{W} \sum_{i=x-\frac{B}{2}}^{x+\frac{B}{2}} \sum_{j=y-\frac{B}{2}}^{y+\frac{B}{2}} w(i-x, y-j)\, src(i,j) - C \tag{6}$$

where W is the sum of Gaussian weights w, and C is the adjustment parameter that needs to be adjusted through experiments according to image characteristics and desired results. Through the comparative experiment of grid search with a step size of 7 within a reasonable range of parameters, 28 is the best in the proposed algorithm. According to $T(x,y)$, binarises each pixel (x,y) in the image using $dst(x,y)$, where *maxValue* is taken as 255, to obtain the local binarised image block $Block^{th}(c_x, r_y)$, as equation 7.

$$Block^{th} : dst(x,y) = \begin{cases} maxValue, & \text{if } src(x,y) > T(x,y) \\ 0 & , \text{ otherwise} \end{cases} \tag{7}$$

Finally, store the obtained $Block^{th}(c_x, r_y)$ into the binarisation result in image $M(x,y)$. Repeat the above steps along the path $L(c_x, r_y)$ to obtain the binarised image M and segmented binary blocks $Block^{th}$.

2.4 Image sparsity evaluation

Matrix Sparsity refers to the proportion of non-zero elements in a matrix, where a smaller value indicates a sparser matrix (Duff, 1977). Based on the basic idea of matrix sparsity combined with image blocking and position encoding methods, the image is processed into a matrix with pixel values as elements (Sun and Xu, 2021). Then, the blank background features of the image can be represented by the sparsity of elements in the matrix. Extracting sparsity features from image blocks and reconstructed images enables the assessment of image sparsity. The schematic diagram of the block image sparsity evaluation algorithm is shown in Figure 3.

Figure 3 Schematic diagram of the image sparsity feature extraction algorithm (see online version for colours)

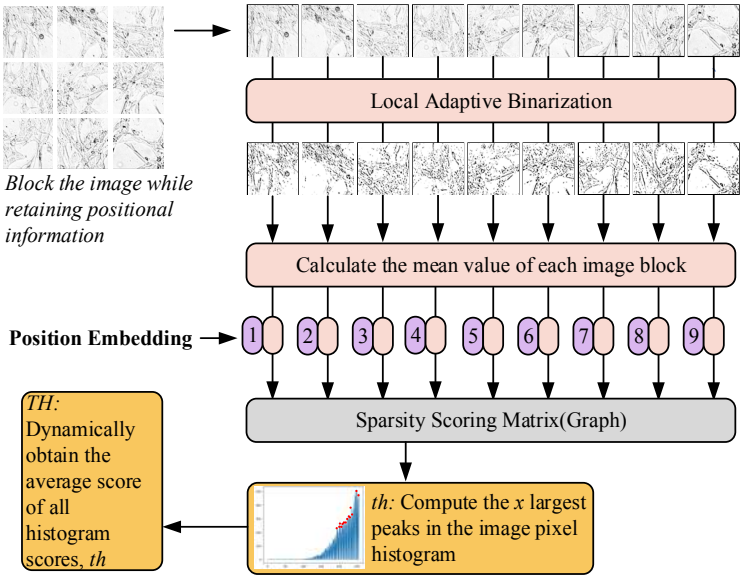

2.4.1 Extracting sub-block block sparse features

Let $S=\left[b_{i,j}\right]_{n\times n}=\left[B_1,B_2,\cdots,B_m\right]$ be the image matrix composed of m binarised $Block^{th}$ sub-blocks $B_1,B_2,\cdots,B_m$, wherein the parameter (i,j) is the position information retained when partitioning the image into blocks. The pixels in the *Block* sub-block are the elements of the matrix. Solve for its matrix sparsity $s_{i,j}$ as shown in equation (8):

$$s_{i,j}=\frac{\sqrt{n^2}-\left\|b_{i,j}\right\|_1/\left\|b_{i,j}\right\|_2}{\sqrt{n^2}-1} \tag{8}$$

where n^2 is the matrix dimension, $\left\|b_{i,j}\right\|_1$ is the L1 norm of the sub-block matrix, and $\left\|b_{i,j}\right\|_2$ is the L2 norm of the sub-block matrix. The sparsity $s_{i,j}$ results are distributed in the interval $[0,1]$. The closer the result is to 0, the sparser the matrix and the lower the proportion of blank background in the *Block* sub-block. The closer to 1, the higher the proportion of blank background in the *Block* sub-block.

Based on the position encoding list $P=[(c,r)_1,(c,r)_2,\ldots,(c,r)_m]$ of the *Block* sub-blocks, construct the sparsity value matrix $m=\left[s_{i,j}\right]$, and map the results of the sparsity value matrix to the interval $[0,255]$ to obtain the image sparsity scoring matrix, also known as the image sparsity scoring map $M=m\times 255=\left[s_{i,j}\right]\times 255$. The sparsity scoring map is approximately a thumbnail of the original image with a scale ratio of

$n^2 : image.shape$, where $image.shape$ is the pixel size of the original image. The more image information there is, the closer the elements in the sparsity scoring matrix are to 0. The more significant the proportion of blank areas, the closer the elements are to 255. The image sparsity is further derived from the sparsity scoring matrix through the scoring map evaluation scale *TH*. A flowchart illustrating the process of dynamically determining the image sparsity evaluation threshold *TH* is shown in Figure 4.

Figure 4 Flowchart of dynamically obtaining the image sparsity evaluation *TH* (see online version for colours)

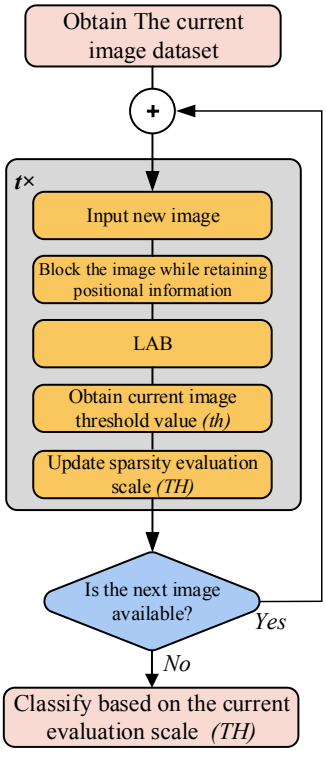

2.4.2 *Dynamically solving the scoring map evaluation scale TH*

The acquired cell images must be input sequentially into the classifier in actual applications for monitoring cell contamination status. Suppose the evaluation scale *TH* acquired when the cell status categories in the image dataset are insufficient is applied to the enriched datasets over increasing culture time. In that case, issues of unstable and inaccurate classification results will occur. The essence of the evaluation scale *TH* is to detect whether the proportion of *Block* sub-blocks with mostly blank background information has reached the threshold condition to determine the image as sparse from a preset degree. Meanwhile, to improve the algorithm's generalisation ability and solve dataset shift problems, the scoring map evaluation scale *TH* will be dynamically determined as the dataset updates. Experiments show that the evaluation scale can be dynamically determined through the histogram of the image dataset.

Let h be the histogram information of the sparsity scoring map M, and $h(i)$ be the number of pixels with pixel value i, where $i \in \{0,1,\ldots,255\}$. Let E be the extremum list, i.e., $E = \{i \mid h(i) > h(i-1) \wedge h(i) > h(i+1)\}$, where $i \in \{1,2,\ldots 254\}$. Then there exists $Manximal_i$ as the list of the most significant x extremum values and their corresponding pixel values, i.e., $Manximal = \{(h(i), i) \mid i \in E\}$, sorted in descending order of $h(i)$, taking the first x elements. Take $a = \{h(i) / \sum_{x=0}^{i} h(i) \mid i \in E\}$ as the weight parameter of pixel value i. The principle of value selection is shown in Figure 5.

Figure 5 Schematic diagram of the n largest maxima values of the scoring pixel histogram (see online version for colours)

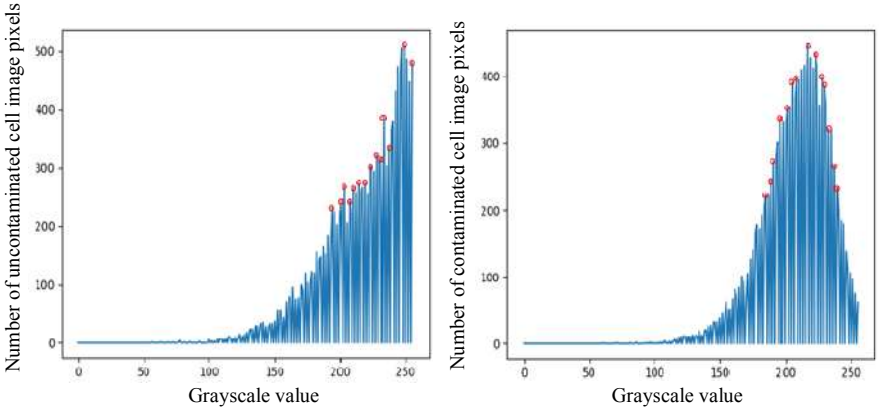

Let X_t represent the image acquired at time t, $M(X_t)$ represent its sparsity scoring map, and Th_t represents its evaluation scale component. Then the evaluation scale calculation at time t is as shown in equation (9):

$$TH_t = \frac{1}{t \times n} \sum_{x=1}^{t} \sum_{i=1}^{n} a_{xi} Manximal_{xi} = \frac{1}{t} \sum_{x=0}^{t} Th_x \tag{9}$$

When dynamically acquiring the evaluation scale, whenever a new image X_{t+1} is acquired, its evaluation scale component Th_{t+1} is calculated, then the evaluation scale is updated to $TH_{t+1} = \frac{1}{t+1} \sum_{x=1}^{t+1} Th_x$. The sparsity scoring map is binarised globally with this evaluation scale as the threshold, calculated as shown in equation (10):

$$C_{i,j} = \begin{cases} max\ Value, & m_{i,j} \le TH_t \\ 0, & m_{i,j} > TH_t \end{cases} \tag{10}$$

where $C_{i,j}$ is the binarised result for pixel $x(i,j)$ in the scoring map, solving for the sparsity of the matrix composed of $C_{i,j}$ as elements to obtain the image sparsity evaluation Sm, calculated as shown in equation (11):

$$Sparse\ Matrix:\ Sm = \frac{\sum_{x=1}^{i}\sum_{y=1}^{j} C_{x,y}}{i \times j} \tag{11}$$

In the scoring map, pixel values lower than the threshold *TH* represent that the mean pixel value of the corresponding *Block* sub-block of the original image is lower than the evaluation scale *TH*. This means the proportion of blank areas in that *Block* has yet to reach the requirement, and we can infer that the region of the cell image is not contaminated. The sparse features of the blank background in the image can be effectively reflected by evaluating all *Block*, i.e., binarising the scoring map using the evaluation scale *TH* as a threshold. Then, the mean pixel value of the binarised scoring map is calculated as the image sparsity evaluation.

2.5 Image sparsity feature clustering

In contaminated cell images, the image sparsity value is lower when the proportion of blank background is deficient. Image sparsity can be utilised to differentiate images contaminated to various degrees. *K*-means clustering is a conventional unsupervised clustering approach where the data input into the classifier typically requires two or more features. Let the image sparsity evaluation feature $Sm_i \in \{a \mid 0 \le a \le 255\}$ be the primary feature, and select the feature with the fewest outliers from the shallow image features as the secondary feature denoted by f_i. Let $K = \{(Sm_i, f_i) \mid i = 1, 2, \ldots, t\}$ represent all the features of the image dataset at time t. Experiments comparing the classification effects of two types of shallow image features demonstrate that the standard deviation of pixels in the sparsity-scoring image has the fewest outliers, thus designating it as our chosen secondary feature f_i.

The *K*-means clustering classification process calculates the Euclidean distance between each sample and cluster center without considering the significance of each dimension. When K is input directly into the classifier, even if the image sparsity feature Sm_i has a substantial interval in the little values range, its importance in partitioning the clustering result may be obscured due to the influence of other dimensions. Consequently, this approach fails to achieve optimal classification within an ideal numerical range. Using normalised scale scaling techniques can increase the classification weight of the little values range of image sparsity values and diminish the impact of secondary dimensions. Apply logarithmic normalisation to each feature Sm_i, denoted as $SM_i = log_{255}(Sm_i)$, where SM_i represents the normalised feature. Implement min-max normalisation on each feature f_i, denoted a $F_i = \frac{f_i - min(f)}{max(f) - min(f)}$, where F_i represents the normalised feature. Input the processed features SM_i and F_i into the *K*-means clustering classifier to acquire the clustering outcomes $C = \{c_i \mid i = 1, 2, \ldots, n\}$, where c_i signifies the cluster label of the *i*th data. Since there are only two labels of contaminated and uncontaminated in the classification results, set the number of cluster centers to 2.

3 Experiments

3.1 Experimental environment

The experimental environment in this study was based on the Windows 10 operating system. The Anaconda 2.3.1 distribution was utilised for managing the Python 3.9.16 interpreter and relevant scientific computing packages, while PyCharm 2023.1.2 professional integrated development environment facilitated the coding and execution of Python scripts for extracting image sparsity as a primary feature in *K*-means clustering classification experiments conducted on leukocyte cell images cultured in vitro.

The evaluation of clustering results encompassed accuracy (ACC) (Van Gansbeke et al., 2020; Chen et al., 2020), adjusted rand index (ARI) (Ciortan and Defrance, 2021; Peyvandipour et al., 2020; Mirsadeghi et al., 2021), normalised mutual information (NMI) (Peyvandipour et al., 2020; Van Gansbeke et al., 2020), homogeneity, completeness, V-score (Mirsadeghi et al., 2021), and running time from seven perspectives.

3.2 Dataset

The dataset of in vitro cultured leukocyte cells comprises 852 images of uncontaminated cells obtained from multiple culture cycles and 224 images of contaminated cells from the same cycles. In total, there are 1076 high-resolution (1920×1080 ppi) images available. To expand the dataset, the 224 contaminated images were subjected to rotation, inversion, and scaling techniques in order to augment the dataset, thereby simulating real experimental conditions. Consequently, the final dataset consists of 1368 cell images exhibiting various conditions such as uneven illumination, blurring, noise, inconsistent scaling, and low contrast. Figure 6 showcases some representative samples featuring complex backgrounds.

Figure 6 The images of partially cultured cells in vitro under complex conditions: (a) uneven illumination; (b) blur and ghosting; (c) high noise; (d) inconsistent scaling; (e) low contrast and (f) shadow occlusion (see online version for colours)

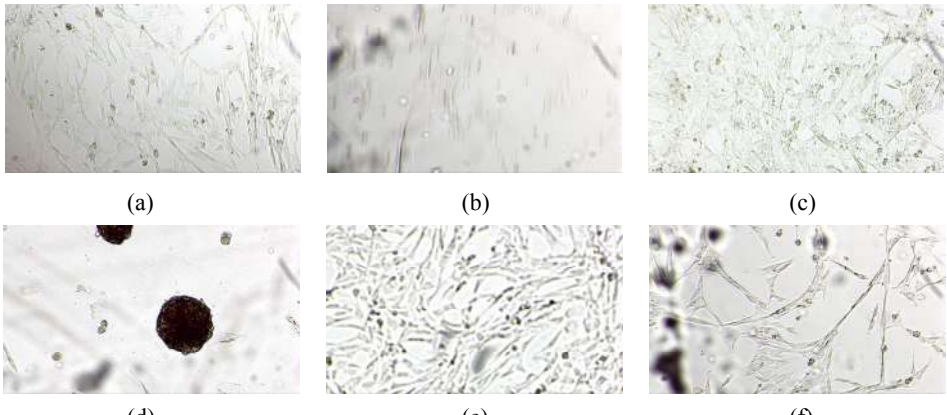

(a) (b) (c)

(d) (e) (f)

Distinguishing between the two types of images using low-level visual features and statistical features, such as information entropy, central tendency (mode and median),

distribution shape (skewness and kurtosis), degree of dispersion (mode-median ratio, quartile range, range, mean difference, and standard deviation) is challenging. After consistent preprocessing involving greyscale transformation and sharpening, the shallow feature parameter values of the two categories of cell images were taken as data points, and the mean value for each feature was computed. As shown in Figure 7, there is a notable intersection between the distribution ranges of the shallow features of the two types of cell images. Additionally, these distribution ranges intersect with the mean lines of the other class, indicating the absence of a clear boundary between the two image types. Therefore, it is necessary to establish more abstract and advanced features to classify the two types of images.

Figure 7 Comparison of shallow features of two classes of images (see online version for colours)

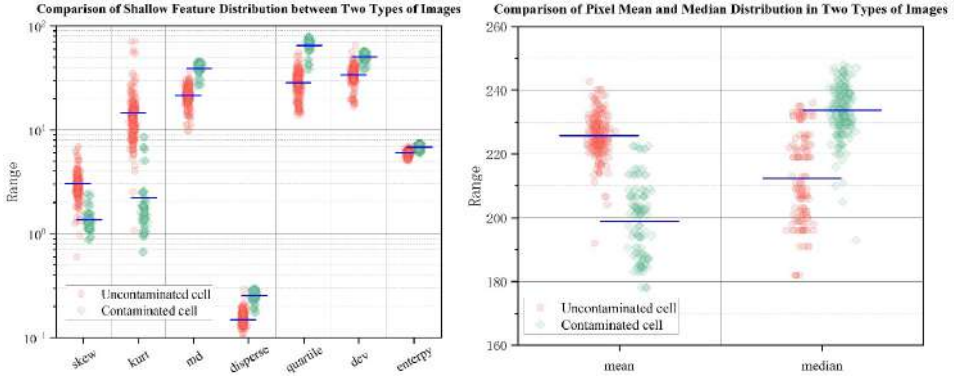

Figure 8 Comparison of greyscale images between two classes: (a) images of contaminated cells and (b) images of uncontaminated cells (see online version for colours)

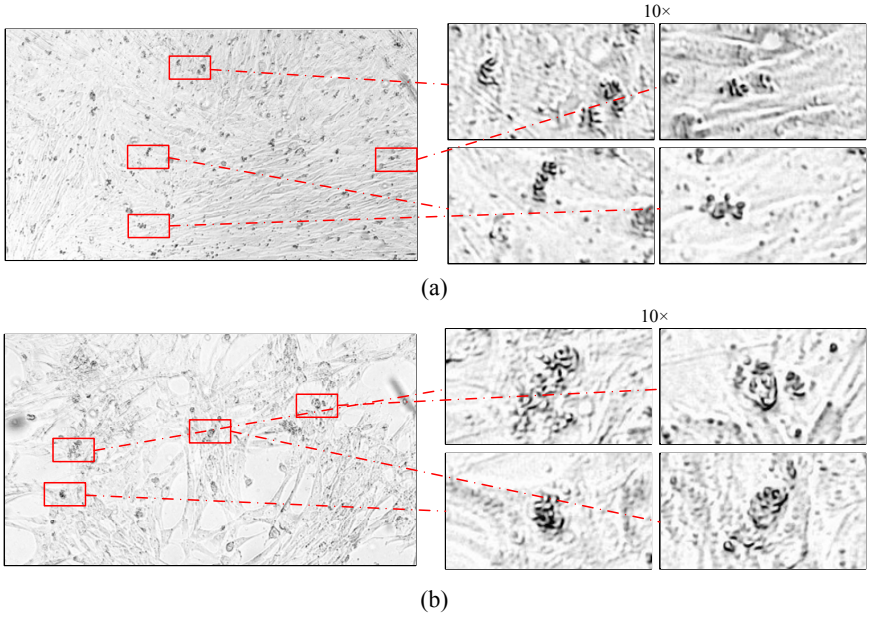

In the dataset, cell images with longer culture times and contaminated cell images have high similarity in salient pixels and statistical features, with no apparent differences. In leukocyte cell in vitro culture experiments, leukocyte cells demonstrate a fusiform, adherent morphology. During the initial stage of bacterial contamination ($t < 2h$), dark scattered dots can be observed, which is the morphology of an individual or a few clustered bacteria. Since microorganisms grow more rapidly than cells and can produce toxins that affect cell growth or even cause death, adherent cells will collapse, detach from the wall, and suspend in the culture medium. The culture medium becomes turbid with no observable transparent background. Sometimes, no turbidity can be seen when the culture medium is still, but slight shaking will make many turbid substances float. As the duration of contamination increases ($2h < t < 4h$), contaminated bacteria gradually aggregate and encircle the periphery of proliferating cells. With persistent contamination($6h < t$), most cells become enveloped by bacteria, posing challenges in discerning cell morphology due to their dense clustering.

Following cell contamination, during the limited remediation period of 48 h to eliminate the source of contamination, it becomes challenging to differentiate between contaminated and uncontaminated cells using deep learning methods designed for bacterial detection due to the presence of light yellow or black small dots, these dark spots may comprise nuclei and cytoplasmic granules, which can be misleading, with similar structures in both types of cell images. Representative cell images are presented in Figure 8.

3.3 Experimental results and analysis

3.3.1 Algorithm parameter optimisation

The Taguchi orthogonal method explores the impact of image block size n and the binarisation threshold TH determined by x largest extremum for judging sparsity degree on image segmentation effects during the image sparsity scoring map acquisition process. By initially marking potential blank background regions in the training image dataset and measuring the determined pixel area occupied by these identified blank background regions, it was observed that the largest enclosed blank background area did not exceed 64 ppi. Therefore, the image block size value must only traverse the $[2,64]$ interval, and the binarisation threshold value traverses the $[0,255]$ interval. Each parameter pair (n,TH) will produce a set of image sparsity values Sm_i, and sorting the image labels in ascending order of Sm_i gives the list $S_{(n,TH)} = [(Sm_{min}, Label_a), (Sm_i, Label_a), \ldots, (Sm_{max}, Label_b)]$, where $Label$ is the true label of the image category. Suppose the two types of labels in the list $S_{(n,TH)}$ are completely separated by a clear boundary. In that case, the classification effect of the parameters can be determined by the sparsity interval ratio R_i.

Suppose in $S_{(n,TH)}$ the image sparsity interval (Sm_a, Sm_{a+1}) that achieves complete classification is between image a and image $a+1$. The sparsity interval here is $D_a = Sm_{a+1} - Sm_a$, and the most significant image sparsity interval except D_a in $S_{(n,TH)}$

is $D_M = max\left(\left\{Sm_{i+1} - Sm_i \mid i \in \{1,2,\ldots,t-1\} \wedge i \neq a\right\}\right)$. Then the sparsity interval ratio can be obtained as $R_i = \left(D_a - D_M\right)/D_M$. The sparsity interval ratio has a value, there is a boundary that makes the two classes of images completely classified. A larger ratio means the boundary between the two types of images in sparsity is more prominent, thus achieving more accurate classification. 20% of the dataset's images are used as training set for parameter tuning. Figure 9 shows the distribution of sparsity interval ratios R_i sorted by the size order of image block size n and binarisation threshold *TH*.

Figure 9 Algorithm parameter optimisation (see online version for colours)

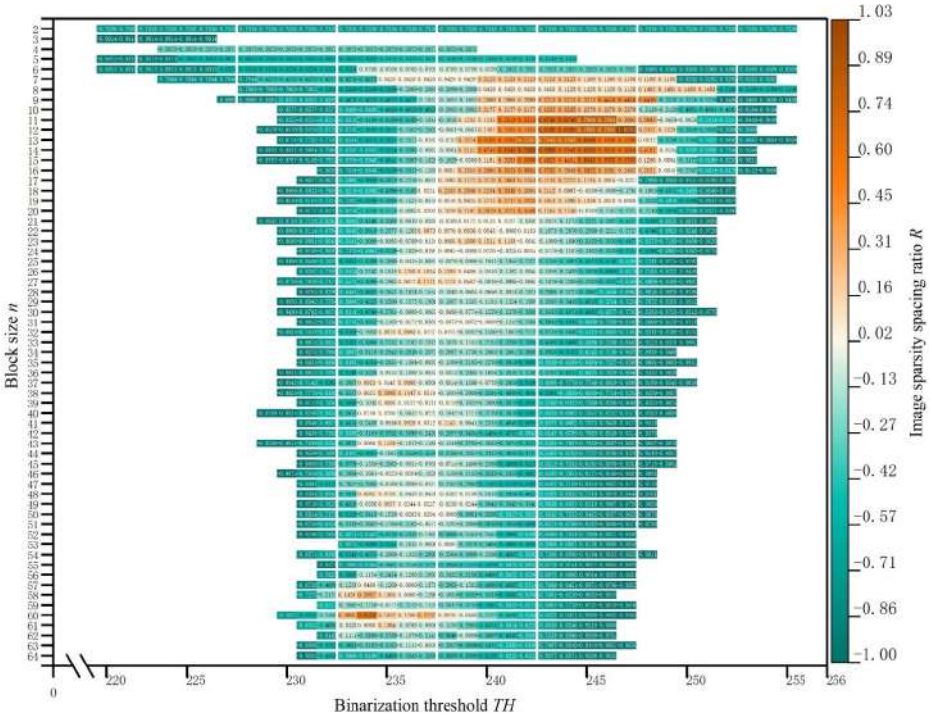

As depicted in Figure 9, when the binarisation threshold TH is less than 246, a boundary that entirely separates the two types of images cannot be found. However, when the image block size is selected within the $[6,64]$ interval, and the binarisation threshold is within the $[233,246]$ interval, suitable boundaries exist that completely separate the two types of images. However, the relative size of the classification boundary interval determines the robustness of the classification effect. Small boundary intervals have randomness on the dataset. Therefore, this paper chooses the parameter pair $\{n=12, TH=246\}$ with the maximum sparsity interval ratio R_i as the parameters for obtaining image sparsity.

3.3.2 Comparative experiments

In order to assess the performance of unsupervised traditional image classification algorithms based on image sparsity in the binary classification problem of contaminated leukocyte cell images in vitro culture, we utilised the aforementioned cell image datasets and experimental methods, along with principal component analysis (PCA-SIFT, PCA-HOG) (Celik, 2009; Duff, 1977). Additionally, we employed six different methods including SSC-MIL (Li et al., 2019), NMF (Gan et al., 2021), DEC (Lu and Li, 2022), information entropy (Chen et al., 2022) for comparative experiments. The classification results were evaluated using silhouette score (Ciortan and Defrance, 2021) and are presented in Figure 10. Figure 10(a)–(g) are, respectively, the clustering result scatter plots of PCA-SIFT, PCA-HOG, SSC-MIL, NMF, DEC, Information Entropy, and SMC algorithms combining image feature extraction and *K*-means clustering methods on images of leukocyte culture in vitro. The background colour in the scatter plot represents the true labels of the image data, while the colour of the dots represents the predicted labels resulting from image data clustering. The dots positioned in the red background correspond to the true labels indicating uncontaminated image data, while those in the blue background represent the true labels indicating contaminated image data. Red dots denote predicted labels for uncontaminated image data, whereas blue dots represent predicted labels for contaminated image data.

Figure 10 Scatter plot of clustering results from different algorithms and silhouette score evaluation plot: (a) *K*-means clustering scatter plot with PCA-SIFT features; (b) *K*-means clustering scatter plot with PCA-HOG features; (c) *K*-means clustering scatter plot with SSC-MIL features; (d) *K*-means clustering scatter plot with NMF features; (e) *K*-means clustering scatter plot with DEC features; (f) *K*-means clustering scatter plot with Information Entropy features; (g) *K*-means clustering scatter plot with SMC features; (h) Silhouette score plot for all algorithms (see online version for colours)

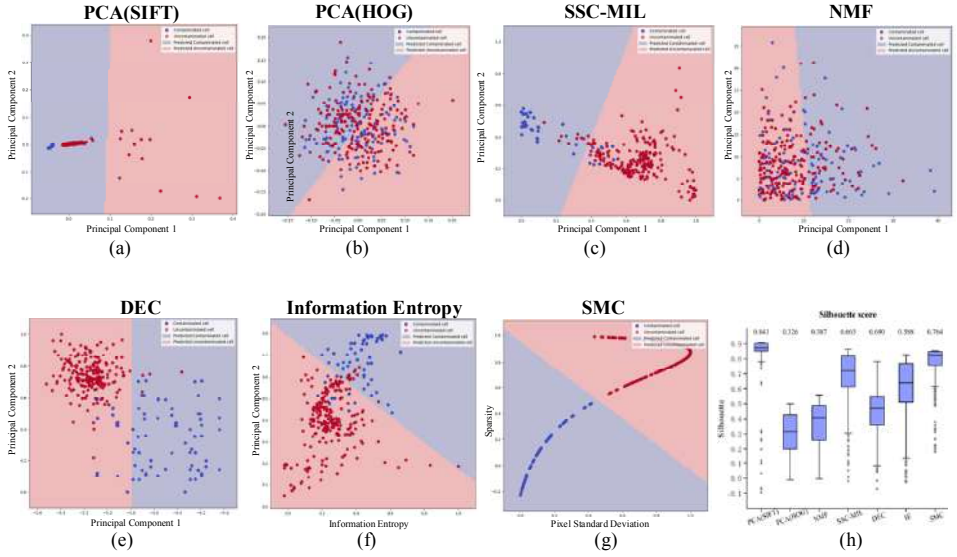

It can be seen from the figures that different image feature extraction methods combined with *K*-means can divide leukocyte cell contamination images in vitro into two

categories, namely standard leukocyte cell images, and contaminated leukocyte cell images. However, there are significant differences in the clustering effects of different combination schemes. The clustering effects of NMF and PCA-HOG feature extraction could be better, with unclear boundaries between the two categories and more misclassified points. The clustering effects of PCA-SIFT, DEC (DAC–Deep Autoencoder-Based Clustering), and SC are better, with more explicit boundaries between the two categories and fewer misclassified points. The clustering effect of SMC is the best, with an apparent boundary between the two categories and virtually no misclassifications. This shows that this experiment's different image feature extraction methods significantly impact the clustering effect. Among them, SMC can extract more compelling and distinctive image features, thus improving the accuracy of clustering results. In the comparison chart of the evaluation metric Silhouette Score, PCA-SIFT has the highest sample similarity within the cluster and the most significant difference from samples in other clusters. SMC algorithm is second, but PCA-SIFT could not be better in other metrics. Table 1 compares the clustering effects of the seven methods.

Table 1 Comparison of clustering evaluation metrics between algorithms

Method/ Evaluation metric	*ACC*	*ARI*	*NMI*	*Homogeneity*	*Completeness*	*V-Score*	*Time/s*
PAC-SIFT	0.416	–0.026	0.048	**0.708**	0.022	0.048	1770.061
PAC-HOG	0.519	–0.001	0.002	0.030	0.116	0.002	175.933
NMF	0.516	0.031	0.012	0.015	0.015	0.015	118.724
SSC-MIL	0.894	**0.863**	**0.774**	0.491	0.506	0.498	3274.613
DEC	0.918	0.695	0.599	0.582	0.617	0.599	140.642
IE	**0.935**	0.588	0.757	0.647	**0.651**	**0.643**	**72.256**
SMC	**0.998**	**0.992**	**0.999**	**0.999**	**0.999**	**0.999**	**86.566**

The image clustering algorithm based on image sparsity evaluation proposed in this paper (SMC) performs excellently in clustering results regarding ACC, reaching 99.8% accuracy and displaying strong classification capability on the dataset. Compared with other methods, the SMC algorithm achieved relatively high values in metrics like silhouette coefficient, ARI, and NMI, exhibiting better clustering effect and consistency with true labels. SMC algorithm also showed relatively high values of inhomogeneity and completeness, further verifying its ability to divide data accurately. Although information entropy feature extraction is faster, its clustering effect is poorer. The proposed method is also relatively short in terms of running time, indicating its efficiency and practicability. In summary, the analysis results based on experimental data show that the proposed method has significant advantages and potential in dataset clustering and can be applied to solve related problems.

4 Conclusions

Based on the basic theory of matrix sparsity, this paper proposes an image sparsity evaluation algorithm combined with a clustering classifier to classify leukocyte cell

contamination. This research conducted an in-depth study and experiments on the problem of leukocyte cell contamination detection. Specifically, the experimental results show that SMC method has advantages in robustness and accuracy when classifying leukocyte cell contamination images in vitro. Compared with other traditional and improved image processing methods, SMC handled situations like limited sample size, low contrast noise, etc. The research results show that traditional image processing methods still have essential application value in specific scenarios. However, deep learning methods have advantages in complex tasks; traditional benefit from fast computing speed, ease of understanding, and mastery. They can still provide good results for simple scenarios or with sufficient training. Therefore, when selecting image processing methods, the complexity of the task and characteristics of the dataset should be considered comprehensively, along with the pros and cons of traditional and deep learning methods. Therefore, future work may combine deep learning with traditional image processing to utilise their complementary strengths.

Acknowledgements

This research was supported by National Natural Science Foundation of China (grant nos. 62373146), Natural Science Foundation of Hunan Province (grant nos. 2022JJ30265), Young Talent of Lifting Engineering for Science and Technology in Hunan Province (2022TJ-Q03), the Key Project of Education Department of Hunan Province of China (23A0382), and the Outstanding Youth Project of Education Department of Hunan Province (22B0476).

References

Bhowmik, S., Sarkar, R., Das, B. and Doermann, D. (2018) 'GiB: a Game theory Inspired Binarization technique for degraded document images', *IEEE Transactions on Image Processing*, Vol. 28, No. 3, pp.1443–1455.

Brînzeu, D.G.T., Feier, V., Herbeck, R., Cristodor, P., Pãunescu, M., Condor, A. and Koreck, A. (2008) 'Microbial and fungal contamination of keratinocyte and fibroblast cell cultures', *Journal of Experimental Medical and Surgical Research*, Vol. 3, pp.123–128.

Celik, T. (2009) 'Unsupervised change detection in satellite images using principal component analysis and k-means clustering', *IEEE Geoscience and Remote Sensing Letters*, Vol. 6, No. 4, pp.772–776.

Chen, C.Y., Huang, Y.C., Wang, Q., Li, G.R. and He, Y.S. (2022) 'Experimental research on automatic object extraction from CT image based on information entropy–taking CT image of dinosaur eggshell slices as an example', *Chinese Journal of Liquid Crystals and Displays*, Vol. 37, No. 07, pp.891–899.

Chen, W., Pu, S., Xie, D., Yang, S., Guo, Y. and Lin, L. (2020) 'Unsupervised image classification for deep representation learning', *Computer Vision–ECCV 2020 Workshops*, *Proceedings, Part II*, 23–28 August, Glasgow, UK, Springer International Publishing, Vol. 16, pp.430–446.

Ciortan, M. and Defrance, M. (2021) 'Contrastive self-supervised clustering of scRNA-seq data', *BMC Bioinformatics*, Vol. 22, No. 1, p280.

Duff, I.S. (1977) 'A survey of sparse matrix research', *Proceedings of the IEEE*, Vol. 65, No. 4, pp.500–535.

Gan, J., Liu, T., Li, L. and Zhang, J. (2021) 'Non-negative matrix factorization: a survey', *The Computer Journal*, Vol. 64, No. 7, pp.1080–1092.

Li, D.X., Wu, Q., Qiu, X. and Liu, Y. (2019) 'Spatial sparse coding based MIL algorithm for criminal investigation image classification', *Journal of University of Electronic Science and Technology of China*, Vol. 48, No. 01, pp.68–73.

Liu, Y., Zhang, H., Zhang, W., Lu, G., Tian, Q. and Ling, N. (2022) 'Few-shot image classification: current status and research trends', *Electronics*, Vol. 11, No. 11, p1752.

Lu, S. and Li, R. (2022) 'DAC–deep autoencoder-based clustering: a general deep learning framework of representation learning', *Intelligent Systems and Applications: Proceedings of the 2021 Intelligent Systems Conference (IntelliSys)*, Vol. 1, Springer International Publishing, pp.205–216.

Mahmood, A. and Ali, S. (2017) 'Microbial and viral contamination of animal and stem cell cultures: common contaminants, detection and elimination', *J. Stem Cell Res. Ther.*, Vol. 2, No. 5, pp.1–8.

Mani, S., Singh, M. and Kumar, A. (2023) *Animal Cell Culture: Principles and Practice*, Springer Nature, Cham, Switzerland.

Mirsadeghi, S.E., Royat, A. and Rezatofighi, H. (2021) 'Unsupervised image segmentation by mutual information maximization and adversarial regularization', *IEEE Robotics and Automation Letters*, Vol. 6, No. 4, pp.6931–6938.

Peyvandipour, A., Shafi, A., Saberian, N. and Draghici, S. (2020) 'Identification of cell types from single cell data using stable clustering', *Scientific Reports*, Vol. 10, No. 1, p12349.

Ray, K., Saharia, S. and Sarma, N. (2021) 'Detection and identification of Ascaris lumbricoides and Necator americanus eggs in microscopic images of faecal samples of pigs', *International Journal of Automation and Control*, Vol. 15, No. 3, pp.378–402.

Sarowar, M.G., Razzak, M.A. and Al Fuad, M.A. (2019) 'HOG feature descriptor based PCA with SVM for efficient and accurate classification of objects in image', *2019 IEEE 9th International Conference on Advanced Computing (IACC)*, IEEE, December, Tiruchirappalli, India, pp.171–175.

Shereena, V.B. and Raju, G. (2022) 'A novel optimised method for speckle reduction in medical ultrasound images', *International Journal of Automation and Control*, Vol. 16, No. 2, pp.137–163.

Sun, S. and Xu, B. (2021) 'Online map fusion system based on sparse point-cloud', *International Journal of Automation and Control*, Vol. 15, Nos. 4–5, pp.585–610.

Van Gansbeke, W., Vandenhende, S., Georgoulis, S., Proesmans, M. and Van Gool, L. (2020) 'Scan: learning to classify images without labels', *European Conference on Computer Vision*, August, Springer International Publishing, Cham, pp.268–285.